ADVANCED FUNCTIONAL MATERIALS

FULL PAPER

DOI: 10.1002/adfm.200700769

An Organic Light-Emitting Diode with Field-Effect Electron Transport**

By *Sarah Schols*,* *Stijn Verlaak*, *Cédric Rolin*, *David Cheyns*, *Jan Genoe*, and *Paul Heremans*

We describe an organic light-emitting diode (OLED) using field-effect to transport electrons. The device is a hybrid between a diode and a field-effect transistor. Compared to conventional OLEDs, the metallic cathode is displaced by one to several micrometers from the light-emitting zone. This micrometer-sized distance can be bridged by electrons with enhanced field-effect mobility. The device is fabricated using poly(triarylamine) (PTAA) as the hole-transport material, tris(8-hydroxyquinoline) aluminum (Alq_3) doped with 4-(dicyanomethylene)-2-methyl-6-(julolindin-4-yl-vinyl)-4H-pyran (DCM_2) as the active light-emitting layer, and *N*,*N*′-ditridecylperylene-3,4,9,10-tetracarboxylic diimide (PTCDI-$C_{13}H_{27}$), as the electron-transport material. The obtained external quantum efficiencies are as high as for conventional OLEDs comprising the same materials. The quantum efficiencies of the new devices are remarkably independent of the current, up to current densities of more than 10 A cm^{-2}. In addition, the absence of a metallic cathode covering the light-emission zone permits top-emission and could reduce optical absorption losses in waveguide structures. These properties may be useful in the future for the fabrication of solid-state high-brightness organic light sources.

1. Introduction

Organic light-emitting devices have attracted much attention since the first report of electroluminescence in a device based on an organic thin film.[1] Over the last decade, remarkable progress has been achieved in the development of organic light-emitting diodes (OLEDs) based on polymers as well as small-molecule semiconductors.[2] It has been shown that the current in OLEDs is typically space charge limited,[3,4] i.e., limited by the bulk of the semiconductor. In other words, the measured current is a drift current determined by the mobility of the charge carriers. The carrier mobility in the organic semiconductor element of OLEDs is typically low.[4,5] To obtain efficient charge transport at reasonable driving voltages, the total thickness of the organic layers in OLEDs is therefore generally limited to 80 to 100 nm.[6] Consequently, light is generated very close (within ca. 50 nm) to the metallic cathode. The proximity of the metal electrode induces severe absorption losses if the OLED is used as a waveguide. This phenomenon has been demonstrated by Andrew et al., who have reported a substantial increase of the lasing threshold of a poly(2-methoxy-5-(2′-ethylhexoxy)-1,4-phenylenevinylene) (MEH-PPV)-based organic laser upon the insertion of a thin silver layer.[7] Reufer et al. have proved that this detrimental waveguide loss caused by metallic layers may be reduced by increased optical confinement.[8] However, this is only possible when the polymer layer is sufficiently thick, in the order of several hundreds of nanometers. The low carrier mobilities of thick organic semiconductor layers give rise to a large electrical resistance, thus precluding the use of thick films in the fabrication of efficient OLEDs. To circumvent this problem, transparent electrodes fabricated from materials such as indium tin oxide (ITO)[9] or aluminum-doped zinc oxide (AZO)[10] have been proposed as alternatives to inject electrons and holes in the organic semiconductor. Yamamoto et al.[11] and Görrn et al.[12] have demonstrated that thin ITO and AZO layers, respectively, can indeed be used as low-loss contacts in waveguide structures. This is mainly because of the much lower optical losses in the visible spectral range for these materials as compared to metallic layers.[13] In addition, Reufer et al. have reported that thick, more conductive ITO layers can also be used for this purpose, provided that a crosslinked hole-transport layer is inserted between the highly conductive ITO and the emission layer.[14]

Recently, light-emitting organic field-effect transistors (LEOFETs) have been proposed as lateral light-emitting devices, complementary to traditional vertical light-emitting diodes. Since these structures combine the optical output of an OLED and the gate control of an organic field-effect transistor in one single device, they may become interesting constructs in the field of organic displays. Displays based on LEOFETs may

[*] S. Schols, Dr. S. Verlaak, C. Rolin, D. Cheyns, Dr. J. Genoe, Prof. P. Heremans
IMEC v.z.w. – SOLO/PME
Kapeldreef 75, 3001 Leuven (Belgium)
E-mail: sarah.schols@imec.be
S. Schols, D. Cheyns, Prof. P. Heremans
Electrical Engineering Department, Katholieke Universiteit Leuven
3001 Leuven (Belgium)
S. Schols
FWO Vlaanderen
Egmontstraat 5, 1000 Brussels (Belgium)

[**] This work is partially supported by the EU-funded Project OLAS (contract No. 015034). The authors thank Merck for PTAA that has been provided through the EU-funded Integrated Project POLYAPPLY (contract No. 507143). S. Schols thanks the FWO Vlaanderen for financial support.

eliminate the difficult integration of an organic light-emitting structure and the organic driving backplane. LEOFETs may also be used to study the optoelectronic performance of organic semiconductors. In contrast to OLEDs where charge transport occurs perpendicularly to the organic layers, charge transport in LEOFETs occurs in the plane and the carriers are transported by field-effect.[15] In field-effect transistors the current flowing between the source and the drain is modulated by applying a bias to a third contact, the gate electrode. In this way, charge carriers can be accumulated or depleted in the semiconductor close to the semiconductor/insulator interface. The gate field provides an additional degree of control over the amount of charge present in the semiconductor. In addition, the accumulated charges can flood deep traps, giving rise to a higher effective mobility for the remaining carriers. The field-effect mobility can be several orders of magnitude higher than the charge carrier mobility in a conventional OLED.[16]

Although the basic concept of a LEOFET dates back from 1996,[17] the development of LEOFETs is still in a relatively embryonic stage. The working principle of a LEOFET is based on the simultaneous injection of electrons and holes into a double or ambipolar layer by tuning of the gate–source and drain–source voltages. The accumulated charge is zero when the biasing conditions are such that the potential at some point in the channel equals the gate potential. Consequently, at this point the electron and hole accumulation layers vanish. Exciton formation occurs near this point and radiative relaxation of these excitons to the ground state leads to light emission. The first LEOFET has been demonstrated by Hepp et al.[18] and is based on vacuum-evaporated tetracene as the organic semiconductor. Since this first demonstration, LEOFETs have been fabricated using polymers,[19,20] small molecules,[21–23] and a heterostructure of p- and n-type organic semiconductors.[24–29] Recent reports in the literature have focused on LEOFETs based on an ambipolar polymeric semiconductor.[30,31] An overview of light-emitting organic transistors has also been recently published.[32]

In LEOFET devices, the charge carriers have a field-effect mobility, and depending on the type of LEOFET, the light-emission zone can be located at some distance from the metallic source and drain electrodes. However, to obtain these properties, three different electrodes need to be used: the source, the drain, and the gate. In addition, most organic field-effect materials demonstrate rather weak photoluminescence; analogously, most organic light-emitting materials show poor field-effect performance.[33] Indeed, a high carrier mobility, which is a prerequisite for transistors, is favored by structural features such as tight intermolecular π-stacking. Examples of suitable materials include pentacene[34] and regioregular poly(3-hexylthiophene) (P3HT).[35] However, the photoluminescence yield is usually low in such materials with strong intermolecular coupling. Conversely, materials exhibiting high photoluminescence quantum yields, for example, poly(p-phenylene vinylene)s (PPVs)[36] are usually characterized by low intermolecular coupling, and therefore limited hopping transport between molecules.[37] Therefore, it would be desirable to form a more elaborate heterojunction consisting of charge transport layers and a light-emitting layer, which can be each optimized separately. Such heterojunction concepts have been used in high-performance OLEDs.[38,39] However, this concept has been difficult to apply to the above-mentioned LEOFET device architectures.

In this paper, a novel two-electrode light-emitting device structure is proposed. The device is a hybrid structure incorporating aspects of both a diode and a field-effect transistor. Compared to conventional OLEDs, the cathode is displaced by one to several micrometers from the light-emission zone. Since the light-emission zone is not covered by metal, the device can be used for top emission or even as a waveguide. The micrometer-sized distance between the cathode and the active region can be bridged by electrons with an enhanced field-effect mobility. Owing to this high charge carrier mobility, large current densities are achievable. The external quantum efficiency at these high current densities is as high as that of conventional OLEDs comprising the same materials. In contrast to LEOFETs, only two electrodes are used in our architecture. Moreover, light emission in our novel device structure always occurs at a fixed position, irrespective of the applied bias, in contrast to the situation in LEOFETs where the emission zone can be moved within the channel by varying the bias conditions.[30,31]

2. Results and Discussion

2.1. Device Fabrication

The schematic architecture of the device is illustrated in Figure 1. The device has been fabricated on top of an ITO-coated glass substrate and comprises an organic hole-transport layer (HTL), an organic light-emitting layer, and an organic electron-transport layer (ETL). Prior to the deposition of these organic layers, an insulating layer of SiO_2 has been deposited by sputtering, covering only part of the ITO surface. ITO serves as the hole-injecting electrode in the device. The cathode has been formed by the deposition of a thin layer of 0.6 nm LiF followed by the deposition of 100 nm Al. This cathode has been

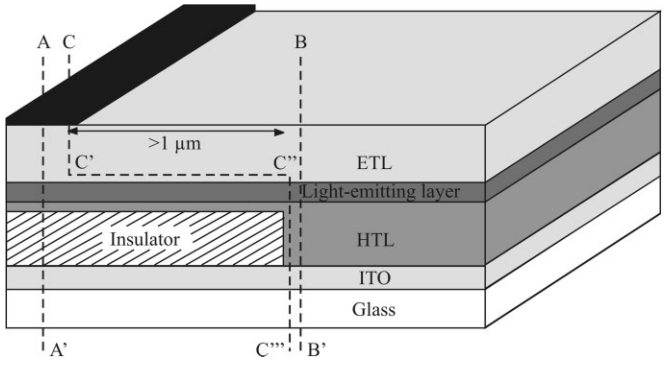

Figure 1. Schematic architecture of the OLED exhibiting field-effect electron transport. The device comprises an organic hole-transport layer, an organic electron-transport layer, and an organic light-emitting layer. The dashed lines AA′, BB′, and CC′C″C‴ indicate three different cross-sctions.

not positioned vertically above the ITO anode in the trench of the SiO_2 insulator. Instead, it has been located directly above the insulator, as shown in Figure 1. The distance between the metallic top electrode and the insulator edge ranges from one to several micrometers. Accurate alignment of the metallic cathode has been achieved by using an integrated shadow mask technique[40] and the angled deposition of the LiF/Al layer (Fig. 2).

The integrated shadow mask has been obtained by patterning a 20 μm thick negative photoresist SU8-25. The different organic layers have been deposited after application and patterning of the SU8-25 resist. After deposition of the organic layers, the sample is mounted on a triangular sample holder and loaded in an ultra high vacuum system to evaporate the cathode. During this deposition process the flux has been maintained at a 45° angle with respect to the substrate. The SU8-25 profile thus creates a shadowed region with a span similar to the thickness of the SU8-25 such that the substrate is only partially covered with the metal. Figure 3 shows a scanning electron microscopy (SEM) image of the device structure. The shadowed region where no metal has been deposited is clearly discernible. It is also clearly apparent that the walls of the SU8-25 layer are slightly re-entrant (i.e., negatively sloped), which is typical for negative photoresists.

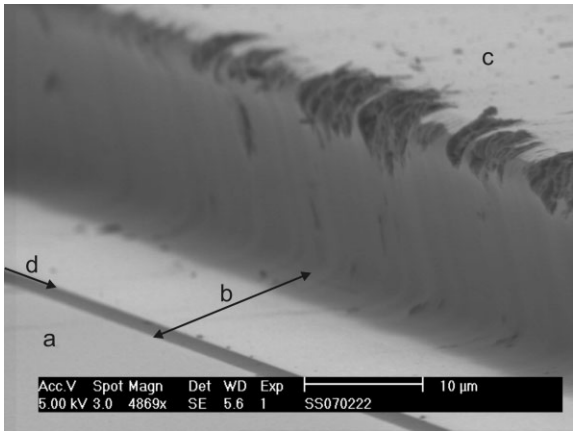

Figure 3. Scanning electron microscopy image of the device structure. a) Metallic cathode, b) shadowed region where no metal is deposited, c) the 20 μm thick SU8-25 layer, and d) arrow indicating the insulator edge.

The molecular structures of the organic materials used to fabricate the device are shown in Figure 4. Poly(triarylamine) (PTAA)[41] has been selected as the hole-transport material. PTAA can be deposited by spin-coating, which yields a film with a smooth top surface that is favorable for the deposition of an additional layer. The bulk hole mobility of PTAA is approximately 10^{-2} cm^2 V^{-1} s^{-1}.[41] The active light-emitting layer is formed by tris(8-hydroxyquinoline) aluminum (Alq_3) doped with 2% of 4-(dicyanomethylene)-2-methyl-6-(julolindin-4-yl-vinyl)-4H-pyran (DCM_2). DCM_2 is a well-known red-light-emitting fluorescent dye used in OLEDs.[42] The photoluminescence quantum yield of this dye family is about 40%.[43] The electron-transport material has been chosen based on the two criteria that are important in our device architecture. First, the organic electron-transport material should have a high electron field-effect mobility since this mobility determines the performance of the device. Secondly, since the electron transport is intended to occur at the heterojunction between the ETL and the light-emitting layer, the lowest unoccupied molecular orbital (LUMO) of the electron-transport material should be slightly lower than the LUMO of Alq_3 and DCM_2. *N*,*N*′-ditridecylperylene-3,4,9,10-tetracarboxylic diimide (PTCDI-$C_{13}H_{27}$) satisfies these two conditions and has therefore been used as the electron-transport material. Gundlach et al. have reported a field-effect mobility of about 0.6 cm^2 V^{-1} s^{-1} for PTCDI-$C_{13}H_{27}$ using Cr top-contacts.[44] A mobility of 0.28 cm^2 V^{-1} s^{-1} has been obtained using LiF/Al top-contacts. Even higher field-effect mobilities can be achieved by annealing after fabrication.[45] The energy levels of the highest occupied molecular orbital (HOMO) and LUMO of PTAA,[41] Alq_3,[46] DCM_2,[47] and PTCDI-$C_{13}H_{27}$[48] are schematically depicted in Figure 4e.

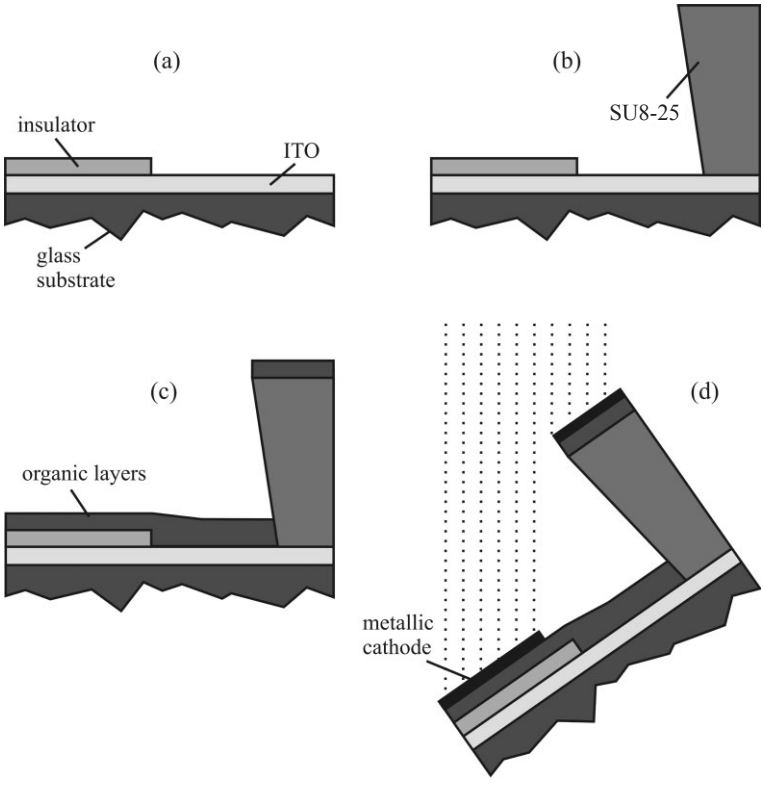

Figure 2. Schematic depiction of the processing sequence for the fabrication of the light-emitting field-effect device structure: a) situation before creation of the integrated shadow mask, b) deposition of the integrated shadow mask, c) deposition of the organic layers, and d) deposition of the metallic cathode with the substrate mounted on a triangular sample holder. During this deposition process, the atomic flux is at a 45° angle with respect to the substrate.

ADVANCED FUNCTIONAL MATERIALS

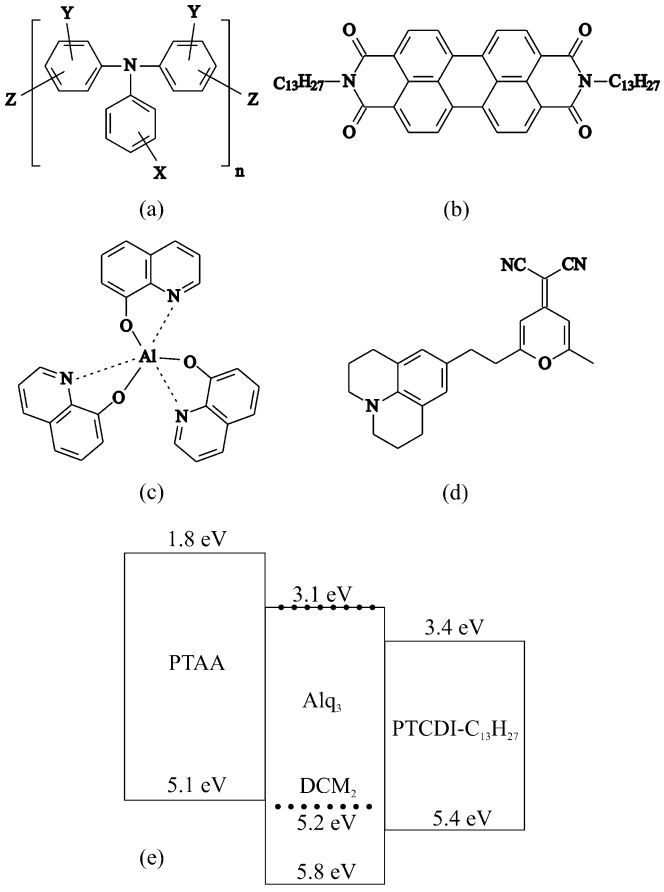

Figure 4. Molecular structure of the organic materials used to fabricate the light-emitting device: a) PTAA, b) PTCDI-$C_{13}H_{27}$, c) Alq_3, and d) DCM_2. e) Energy level diagram for these materials. The dotted lines indicate the highest occupied molecular orbital (HOMO) and the lowest unoccupied molecular orbital (LUMO) positions of DCM_2.

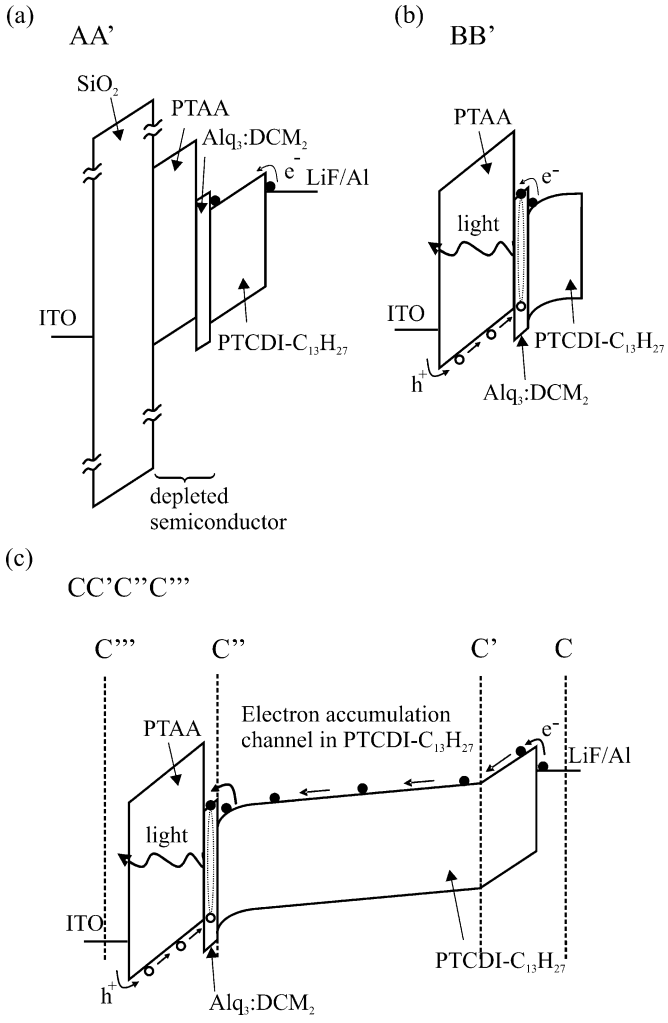

Figure 5. Band diagrams for the device under forward bias conditions through different sections of Fig. 1: a) AA′, b) BB′, and c) CC′C″C‴ cross sections.

2.2. Device Operation

To explain the device operation, in Figure 5 we show the band diagrams through sections AA′, BB′, and CC′C″C‴ of Figure 1 for the device in forward bias, i.e., for a positive anode-to-cathode bias. Under these conditions, electrons are injected from the cathode into PTCDI-$C_{13}H_{27}$ at the cross-section AA′. The semiconductor PTAA and the light-emitting layer Alq_3:DCM_2 on top of the SiO_2 (cross-section AA′) are depleted of holes. As further discussed below, the LUMO offset at the interface between Alq_3 and PTCDI-$C_{13}H_{27}$ prohibits electron injection from PTCDI-$C_{13}H_{27}$ into Alq_3 in the AA′ cross-section. As a result, the depleted PTAA and Alq_3:DCM_2 layers on top of the SiO_2 insulator behave as a combined dielectric layer in series with the SiO_2 insulator, and an electron accumulation layer is formed in the PTCDI-$C_{13}H_{27}$ layer at the interface with Alq_3:DCM_2. These electrons are transported laterally by the electric field from the cathode towards the SiO_2 edge (from C′ to C″). The field-effect mobility of these charge carriers is larger than the charge carrier mobility of a conventional OLED, making transport over several micrometers possible. Near the insulator edge, at position C″, electrons are injected into the Alq_3:DCM_2 layer, where they recombine with holes that are injected from the ITO and transported vertically through the PTAA (see cross section BB′ in Fig. 5). The electron injection at position C″ into Alq_3 is enabled by an enhanced vertical electric field at that position. The enhancement of the vertical field at C″ has two different origins: first, the vertical and lateral electric fields in the channel (section C′C″) collapse into only a vertical field at position C″; furthermore, the presence of a space charge of holes in PTAA increases the vertical electric field that attracts electrons to be injected in the Alq_3:DCM_2 layer. This latter behavior is similar to the enhanced hole injection as a result of the space charge of electrons at the anode of OLEDs reported by Van Woudenbergh et al.[49] Exciton formation occurs and radiative relaxation of these excitons to the ground state results in light emission near the SiO_2 edge, at a micrometer-sized distance from the metallic contact. As a result, this heterojunction device allows the minimization of optical losses at the metal cathode. The vicinity of the ITO bottom-contact is of minor importance with re-

spect to absorption losses because it has been shown that thin transparent ITO layers have low optical losses in the 550–750 nm spectral range.[13]

We have confirmed this view of the device operation by measuring the characteristics of several control devices. We have fabricated control transistors comprising the stacks PTAA/PTCDI-$C_{13}H_{27}$ and PTAA/Alq_3:DCM_2/PTCDI-$C_{13}H_{27}$ on a 100 nm thick SiO_2 dielectric using LiF/Al source and drain top-electrodes. For the PTAA/PTCDI-$C_{13}H_{27}$ transistor, we have extracted a field-effect mobility of 0.2 $cm^2\ V^{-1}\ s^{-1}$ for electrons in PTCDI-$C_{13}H_{27}$ at the heterojunction interface with PTAA. It is striking that the hole-transporting organic semiconductor PTAA provides a good growth surface for the electron-conducting PTCDI-$C_{13}H_{27}$, and that the hetero-interface is appropriate for electron transport. This can be attributed to the smooth top surface of PTAA and the formation of a high-quality interface free of electron traps. We infer the latter from the observation that the electron mobility in PTCDI-$C_{13}H_{27}$ transistors on PTAA-coated SiO_2 is the same as that measured in control transistors that have a gate dielectric consisting of SiO_2 coated with poly-*α*-methylstyrene (P*α*MS). P*α*MS is known to provide a high-quality, electron-trap-free surface[50] that allows good electron transport.[51]

Upon the insertion of Alq_3:DCM_2 between PTAA and PTCDI-$C_{13}H_{27}$, the effective saturation field-effect electron mobility drops to 0.08 $cm^2\ V^{-1}\ s^{-1}$. The output and transfer characteristics of this transistor are shown in Figure 6. We have correlated the reduction in mobility to the different growth behavior of PTCDI-$C_{13}H_{27}$ on Alq_3:DCM_2, as compared to growth on a PTAA surface. Figure 7a and b show the morphology of the PTCDI-$C_{13}H_{27}$ layer upon deposition onto PTAA and PTAA/Alq_3:DCM_2 surfaces. PTCDI-$C_{13}H_{27}$ deposited on PTAA/Alq_3:DCM_2 reveals a much rougher topography than PTCDI-$C_{13}H_{27}$ grown on top of PTAA; this correlates well with the lower field-effect mobility. The root mean square (rms) roughness of the PTCDI-$C_{13}H_{27}$ layer is increased from 6.7 to 10.7 nm upon the insertion of an Alq_3:DCM_2 layer. Since both substrates (PTAA and PTAA/Alq_3:DCM_2) are morphologically similar (both are amorphous flat surfaces with the same rms roughness of 0.4 nm), the observed differences in the growth behavior of PTCDI-$C_{13}H_{27}$ likely originate from interfacial energy differences between the PTCDI-$C_{13}H_{27}$ and PTAA and PTCDI-$C_{13}H_{27}$ and Alq_3:DCM_2 combinations.

Additionally, a control transistor has been fabricated comprising PTAA/Alq_3:DCM_2 as the organic layers, to verify whether Alq_3:DCM_2 can be used as the ETL instead of PTCDI-$C_{13}H_{27}$. No field-effect transport of electrons has been observed in this structure. The non-planar molecular structure of Alq_3 apparently prohibits efficient lateral electron transport. This control experiment also proves that electron transport in the transistor comprising the organic stack PTAA/Alq_3:DCM_2/PTCDI-$C_{13}H_{27}$ and in our novel device structure (between positions C′ and C″ in Fig. 1) indeed occurs through PTCDI-$C_{13}H_{27}$ and not via Alq_3:DCM_2.

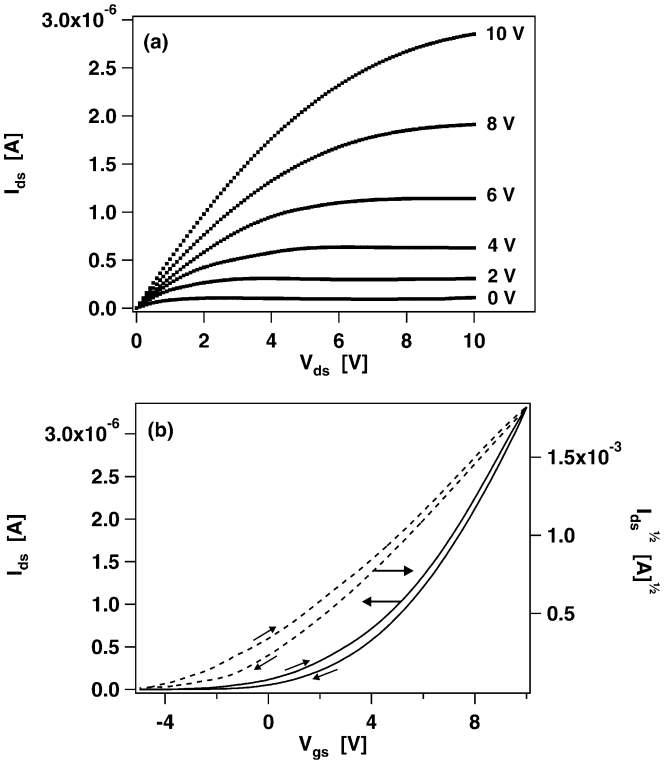

Figure 6. Electrical characteristics of a top-contact transistor comprising PTAA/Alq_3:DCM_2/PTCDI-$C_{13}H_{27}$ as the organic layers (W/L = 2000/50). a) Output characteristics for various gate voltages, and b) transfer characteristics of the same transistor. A saturation mobility of 0.08 $cm^2\ V^{-1}\ s^{-1}$ and a threshold voltage of ca. 0 V are extracted for this device.

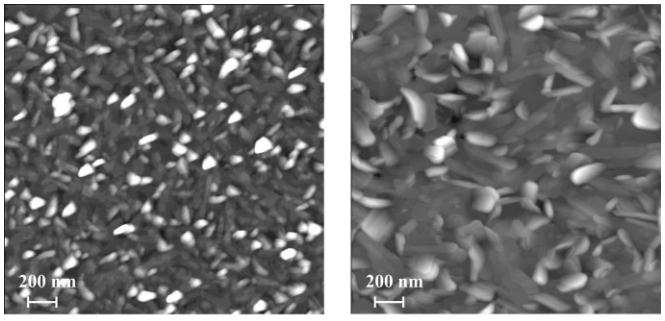

Figure 7. 2 μm × 2 μm atomic force microscopy surface scans of 50 nm thick PTCDI-$C_{13}H_{27}$ layers on top of a) PTAA and b) PTAA/Alq_3:DCM_2. A higher surface roughness is measured for PTAA/Alq_3:DCM_2. The rms roughness is 10.7 nm for PTCDI-$C_{13}H_{27}$ on PTAA/Alq_3:DCM_2 versus 6.7 nm for PTCDI-$C_{13}H_{27}$ grown on PTAA.

2.3. Optical and Electrical Characterization

Figure 8a displays the experimentally measured electrical characteristics of a light-emitting device constructed using the architecture depicted in Figure 1. The device has a width of 1 mm and has been measured under an inert N_2 atmosphere

ADVANCED FUNCTIONAL MATERIALS

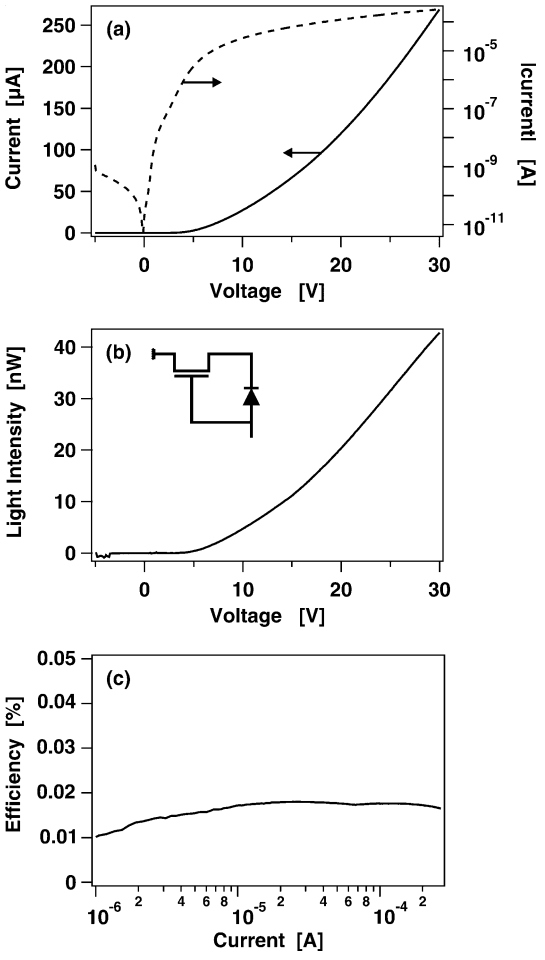

Figure 8. Experimentally measured characteristics of the light-emitting diode with field-effect electron transport. This device has a width of 1 mm and a distance between top electrode and insulator edge of 3.5 μm. a) Current–voltage characteristics, b) corresponding light output. The inset shows the equivalent circuit of this device. c) External quantum efficiency of the device as a function of the current.

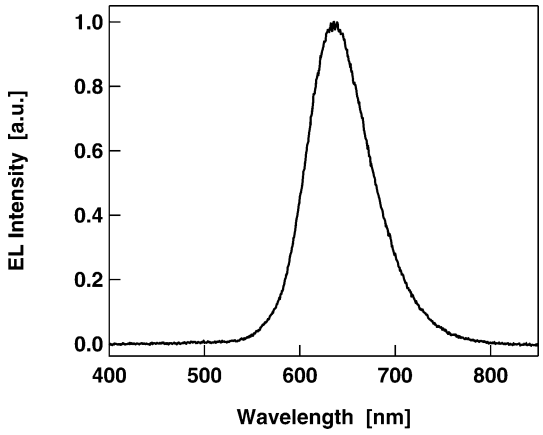

Figure 9. Normalized electroluminescence spectrum of the light-emitting diode with field-effect electron transport. The spectrum corresponds to DCM_2 emission with a maximum positioned at wavelength λ = 636 nm.

immediately after evaporation. The metallic cathode of the device is displaced by 3.5 μm with respect to the insulator edge. Under forward bias, the current increases with increasing voltage. The electrical characteristics can be explained by the equivalent circuit shown in the inset of Figure 8b. This equivalent circuit consists of an n-type transistor with a diode between the gate and the drain.

The device emits red light upon the radiative decay of the excitons. The optical output intensity as a function of the applied voltage bias is shown in Figure 8b. It can be seen that the optical output tracks the current characteristics. The normalized electroluminescence spectrum of the device is shown in Figure 9. The peak emission wavelength is located at 636 nm and corresponds to emission from DCM_2. Two control experiments have enabled us to verify that the observed emission indeed originates from DCM_2. In the first control experiment, we have changed the dye from DCM_2 to $Btp_2Ir(acac)$,[52] a phosphorescent dye with characteristic spectral features that can be easily be recognized. In another control experiment, we have used undoped Alq_3; this device emits green light, peaking at 540 nm, as is characteristic for emission from Alq_3.

In our device structure, the emission zone is well defined and light emission always occurs at a fixed position, namely near the edge of the insulator. This position is independent of the applied bias. The left panel of Figure 10 shows a photograph in reflection of a device without biasing. The metal electrode (white reflecting area) and the insulator edge, indicated by an arrow, are easily discernible. For this device, the distance between the cathode and the insulator edge is 19 μm. The right

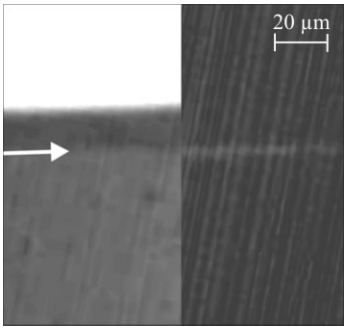

Figure 10. Left panel: Optical microscopy reflection image of a device without bias. The white area is the reflective metal cathode, the arrow indicates the insulator edge. Right panel: Optical microscopy image under forward bias. A narrow line of light appears along the insulator edge. The width of the line is estimated to be about 2 μm.

panel of Figure 10 shows an image of the optical output in the dark when the device is in forward bias. A narrow line of red light appears alongside the edge of the insulator. The light intensity increases with the bias voltage. Despite the narrow emission zone, the red light can easily be observed by the naked eye. The measured width of the emission zone is about 2 μm.

2.4. Analysis

The experimentally observed behavior has been qualitatively verified by numerical simulations. A simplified device, comprising a HTL and a light-emitting ETL, has been simulated using the Silvaco Atlas 2D device simulator. The material parameters used in the simulations are summarized in Table 1. For the ETL, an electron mobility of 8×10^{-2} cm^2 V^{-1} s^{-1} has been used, which corresponds to the experimentally measured electron field-effect mobility of PTCDI-$C_{13}H_{27}$ in our device. The hole mobility of the ETL is taken to be 5×10^{-4} cm^2 V^{-1} s^{-1}. On the other hand, for the HTL, a hole mobility of 5×10^{-3} cm^2 V^{-1} s^{-1} and a negligible electron mobility are assumed. The HOMO and LUMO of the ETL and HTL are assumed to be similar to the HOMO and LUMO of PTCDI-$C_{13}H_{27}$ and PTAA, respectively. Typical values for the singlet lifetime (τ) and exciton diffusion length (L_{diff}) have been obtained from the literature.[53] The top contact is assumed to be located 6 μm from the insulator edge. Figure 11a illustrates the simulated recombination zone as a result of applying a positive bias to the anode. It can be clearly seen that recombination occurs near the insulator edge, several micrometers away from the metallic contact. The simulated recombination zone has a width of about 2 μm, which is consistent with the experimental observations. Figure 11b confirms the presence of an electron accumulation layer at the interface between the HTL and the light-emitting ETL when a positive bias is applied to the anode with respect to the cathode. This electron accumulation region vanishes beyond the insulator edge, since electrons and holes recombine there.

Table 1. Summary of the parameters used in the 2D device simulator.

	HTL	Light-emitting ETL
HOMO [eV]	5.1	5.4
LUMO [eV]	1.8	3.4
μ_e [cm^2 V^{-1} s^{-1}]	1×10^{-7}	8×10^{-2}
μ_h [cm^2 V^{-1} s^{-1}]	5×10^{-3}	5×10^{-4}
L_{diff} [nm]		10
τ [s]		16×10^{-9}

The external quantum efficiency of the fabricated devices has been estimated based on the luminance, electroluminescence spectra, and current. The measured maximum external quantum efficiency of the device is 0.02%, which is similar to that of a light-emitting diode comprising the same materials. Reference OLEDs with Alq_3:DCM_2 active layers have been demonstrated with up to 0.5% efficiency.[42] In these reference OLEDs, Alq_3 is used as the ETL instead of PTCDI-$C_{13}H_{27}$. However, we have not been able to use Alq_3 in our structure because it does not conduct electrons in the thin-film transistor configuration. Further optimization of material combinations is needed to increase the external quantum efficiency.

The light intensity can be tuned by changing the distance between the metallic contact and the insulator edge. We have measured different devices for which the top-contact displacement with respect to the insulator edge is systematically varied from 0.8 to 9 μm. In Figure 12a the measured maximum external quantum efficiency of each of these devices is plotted as a function of the distance between the cathode and the insulator edge. As expected, the maximum external quantum efficiency remains constant. On the other hand, at the maximum breakdown voltage of the SiO_2 insulator (about 30 V), higher currents are possible in devices with shorter cathode displacements with respect to the insulator edge. As a result, the maximum achievable optical output power and brightness can be higher for smaller distances. This is illustrated in Figure 12b, which shows the light intensity of three different devices where the distances between the metallic cathode and the insulator edge are 7.3, 5.1, and 3.5 μm.

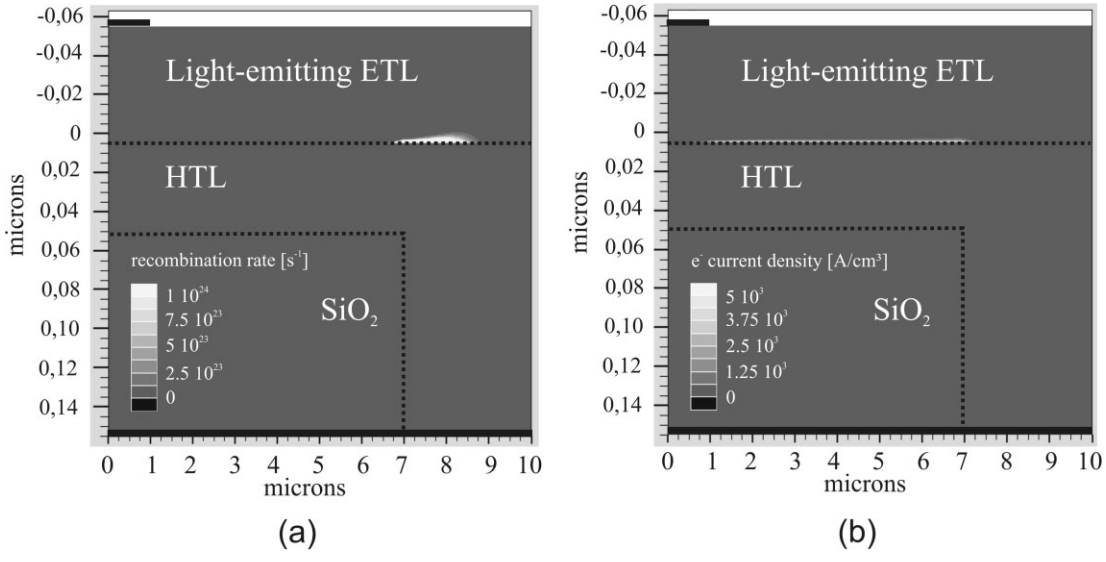

Figure 11. a) The simulated recombination rate and b) the simulated electron accumulation layer under forward bias.

ADVANCED FUNCTIONAL MATERIALS

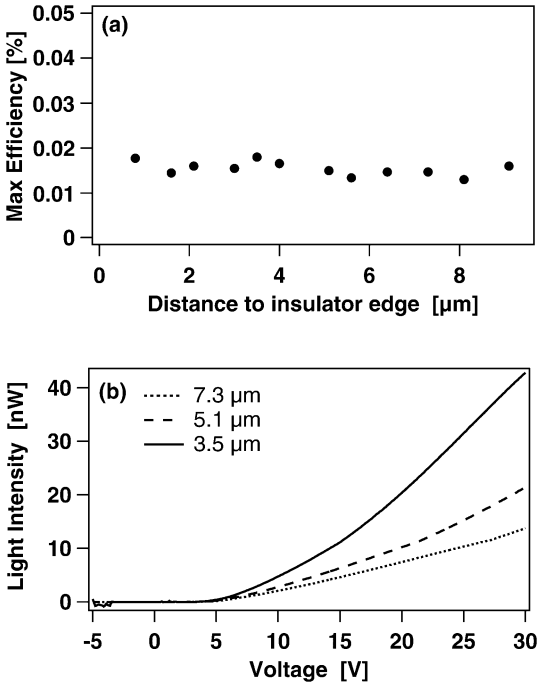

Figure 12. a) The maximum external quantum efficiency as a function of the distance from the insulator edge. The maximum external quantum efficiency is constant irrespective of the distance. b) Light intensity versus applied voltage of three different devices for which the top-contact displacement with respect to the insulator edge is 7.3 μm (dotted lines), 5.1 μm (dashed lines), and 3.5 μm (solid lines).

Taking into account a 2 μm wide emission zone, the maximum hole current density in the device at the breakdown voltage of 30 V is estimated to be 13 A cm^{-2}. This current density is much higher than the current density obtained for conventional OLEDs (typically in the order of 10^{-2} A cm^{-2} at the point of maximum external quantum efficiency). The maximum electron current density in the accumulation layer of the light-emitting device is even higher. Assuming that the current flow is confined to a 1.5 nm thick electron accumulation layer, current densities of 1800 A cm^{-2} are achieved. This is significantly higher than the current densities achieved in ambipolar organic light-emitting transistors reported up till now;[30,31] the improved performance arises from the higher electron mobility of our device. Figure 8c shows the measured external quantum efficiency as a function of the current. No significant roll-off is observed within experimental error up to the maximum current.

3. Conclusions

We have realized an OLED with field-effect electron transport. In our device configuration, the metallic top-contact is remote from the light-emission zone. The micrometer-sized distance between the cathode and the light-emission zone is bridged by electrons with an enhanced field-effect mobility. The light-emission occurs at a fixed position irrespective of the applied bias. We have fabricated this device using Alq_3:DCM_2 as a host–guest light-emitting material system, PTCDI-$C_{13}H_{27}$ as the electron-transport material, and PTAA as the hole-transport material. Light-emission is correlated with the current, and can be modulated by the anode-to-cathode voltage. The measured device operation has been verified by 2D numerical simulations and by the characteristics of a number of control devices. Devices with smaller distances between the cathode and the insulator edge allow for larger currents at the maximum operating voltage, and therefore also yield higher brightness. The external quantum efficiency has been confirmed to be as high as in a conventional OLED comprising the same materials. The quantum efficiency is remarkably constant up to the maximum current, which corresponds to a hole current density on the order of 10 A cm^{-2}. This high current density, in combination with reduced optical absorption losses arising from the remoteness of the metal cathode, may lead to interesting applications as waveguide OLEDs and possibly a laser structure.

4. Experimental

Materials: PTCDI-$C_{13}H_{27}$ and Alq_3 were purchased from Aldrich and purified once by sublimation before loading into an ultra high vacuum system ($p = 10^{-8}$ torr (1 torr = 133.3 Pa)). PTAA, received from Merck, was used as received. DCM_2 was purchased from H. W. Sands and also used without further purification. The integrated shadow mask was realized using SU8-25, which was purchased from MicroChem and used as received.

Device Processing: The devices were fabricated on ITO-coated glass substrates with a sheet resistance of ca. 16 Ω $square^{-1}$. Prior to the deposition of the organic layers, a ca. 100 nm thick insulating SiO_2 layer was deposited on top of ITO by sputtering in a Pfeiffer Spider 630 instrument. The trenches were selectively wet-etched through the SiO_2 to contact the ITO layer, which serves as the hole-injecting electrode. Next, a single layer of negative, epoxy-type, near-UV photoresist SU8-25 was patterned by photolithography to obtain a ca. 20 μm thick layer. This layer was resistant to solvents, acids, and bases and was characterized by excellent thermal stability. Subsequently, the substrate was cleaned with solvents (acetone and isopropanol) and exposed to an UV-ozone ambient for 15 min. Then, PTAA was spin-coated at 1000 rpm on top of the patterned structure. The sample was baked on a hotplate at 110 °C for 20 min after spin-coating to evaporate the solvent. In the next step, a 20 nm thick light-emitting layer was deposited under ultra high vacuum ($p = 10^{-8}$ torr) by co-evaporation of 100:2 (mass ratio) Alq_3 and DCM_2. Subsequently, 50 nm of PTCDI-$C_{13}H_{27}$ was evaporated as the ETL. The deposition rate during evaporation was maintained at 0.5 Å s^{-1}, and the substrate was kept at room temperature. The sample was then mounted on a triangular sample holder followed by the evaporation of 0.8 nm LiF and 100 nm Al. During this deposition process, the flux was maintained at an angle of 45° with respect to the substrate. In this way, the SU8-25 profile created a shadowed region where no LiF and Al were deposited. The shadowed region had a span of about 20 μm, which was similar to the thickness of the SU8-25 layer. All processing steps after UV-ozone treatment were carried out in a dry nitrogen glovebox (<1 ppm O_2, <5 ppm H_2O) or in ultra high vacuum. The glovebox and ultra high vacuum systems were attached to each other. Therefore, samples could be transported from high vacuum to the glovebox and vice versa without exposure to ambient atmosphere.

Device Characterization: The devices were characterized immediately after evaporation in an inert N_2 atmosphere. The electrical characteristics were measured using an Agilent 4156C parameter analyzer. A calibrated integrated sphere (SphereOptics Hoffman GmbH) was

used for light-intensity measurements and external quantum efficiency calculations. To determine the spectral characteristics, the emitted light was detected by means of an optical multichannel analyzer (OMA) in conjunction with a charge coupled device (CCD). These measurements were performed at room temperature in a cryostat to prevent photo-oxidation.

Received: July 13, 2007
Revised: August 31, 2007
Published online: December 18, 2007

[1] C. W. Tang, S. A. VanSlyke, *Appl. Phys. Lett.* **1987**, *51*, 913.
[2] L. S. Hung, C. H. Chen, *Mater. Sci. Eng. R* **2002**, *39*, 143.
[3] M. Pope, C. E. Swenberg, *Electronic Processes in Organic Crystals and Polymers*, Vol.1, 2nd ed., Oxford University Press, New York **1999**, Ch.2.
[4] P. W. M. Blom, M. J. M. de Jong, *IEEE J. Quantum Electron.* **1998**, *4*, 105.
[5] C. Hosokawa, H. Tokailin, H. Higashi, T. Kusumoto, *Appl. Phys. Lett.* **1992**, *60*, 1220.
[6] I. D. Parker, *J. Appl. Phys.* **1994**, *75*, 1656.
[7] P. Andrew, G. A. Turnbull, I. D. W. Samuel, W. L. Barnes, *Appl. Phys. Lett.* **2002**, *81*, 954.
[8] M. Reufer, S. Riechel, J. M. Lupton, J. Feldmann, U. Lemmer, D. Schneider, T. Benstem, T. Dobbertin, W. Kowalsky, A. Gombert, K. Forberich, K. Wittwer, U. Scherf, *Appl. Phys. Lett.* **2004**, *84*, 3262.
[9] G. Parthasarathy, P. E. Burrows, V. Khalfin, V. G. Kozlov, S. R. Forrest, *Appl. Phys. Lett.* **1998**, *72*, 2138.
[10] H. Kim, C. M. Gilmore, J. S. Horwitz, A. Piqué, H. Murata, G. P. Kushto, R. Schlaf, Z. H. Kafafi, D. B. Chrisey, *Appl. Phys. Lett.* **2000**, *76*, 259.
[11] H. Yamamoto, T. Oyamada, H. Sasabe, C. Adachi, *Appl. Phys. Lett.* **2004**, *84*, 1401.
[12] P. Görrn, T. Rabe, T. Riedl, W. Kowalsky, G. Galbrecht, U. Scherf, *Appl. Phys. Lett.* **2006**, *89*, 161 113.
[13] V. G. Kozlov, G. Parthasarathy, P. E. Burrows, V. B. Khalfin, J. Wang, S. Y. Chou, S. R. Forrest, *IEEE J. Quantum Electron.* **2000**, *36*, 18.
[14] M. Reufer, J. Feldmann, P. Rudati, A. Ruhi, D. Müller, K. Meerholz, C. Karnusch, M. Gerken, U. Lemmer, *Appl. Phys. Lett.* **2005**, *86*, 221 102.
[15] F. Dinelli, M. Murgia, P. Levy, M. Cavallini, F. Biscarini, D. M. de Leeuw, *Phys. Rev. Lett.* **2004**, *92*, 116 802.
[16] C. Tanase, E. J. Meijer, P. W. M. Blom, D. M. de Leeuw, *Phys. Rev. Lett.* **2003**, *91*, 216 601.
[17] A. Dodabalapur, H. E. Katz, L. Torsi, *Adv. Mater.* **1996**, *8*, 853.
[18] A. Hepp, H. Heil, W. Weise, M. Ahles, R. Schmechel, H. von Seggern, *Phys. Rev. Lett.* **2003**, *91*, 157 406.
[19] M. Ahles, A. Hepp, R. Schmechel, H. von Seggern, *Appl. Phys. Lett.* **2004**, *84*, 428.
[20] J. Swensen, D. Moses, A. J. Heeger, *Synth. Met.* **2005**, *153*, 53.
[21] T. Oyamada, H. Uchiuzou, S. Akiyama, Y. Oku, N. Shimoji, K. Matsushige, H. Sasabe, C. Adachi, *J. Appl. Phys.* **2005**, *98*, 074 506.
[22] J. Reynaert, D. Cheyns, D. Janssen, R. Müller, V. I. Arkhipov, J. Genoe, G. Borghs, P. Heremans, *J. Appl. Phys.* **2005**, *97*, 114 501.
[23] C. Santato, R. Capelli, M. A. Loi, M. Murgia, F. Cicoira, V. A. L. Roy, P. Stallinga, R. Zamboni, C. Rost, S. F. Karg, M. Muccini, *Synth. Met.* **2004**, *146*, 329.
[24] C. Rost , S. Karg, W. Rieß, M. A. Loi, M. Murgia, M. Muccini, *Appl. Phys. Lett.* **2004**, *85*, 1613.
[25] C. Rost , S. Karg, W. Rieß, M. A. Loi, M. Murgia, M. Muccini, *Synth. Met.* **2004**, *146*, 237.
[26] M. A. Loi, C. Rost, M. Murgia, S. Karg, W. Rieß, M. Muccini, *Adv. Funct. Mater.* **2006**, *16*, 41.
[27] F. Dinelli, R. Capelli, M. A. Loi, M. Muccini, A. Fachetti, T. J. Marks, *Adv. Mater.* **2006**, *18*, 1416.
[28] R. Capelli, F. Dinelli, M. A. Loi, M. Murgia, R. Zamboni, M. Muccini, *J. Phys.: Condens. Matter* **2006**, *18*, S2127.
[29] S. De Vusser, S. Schols, S. Steudel, S. Verlaak, J. Genoe, W. D. Oosterbaan, L. Lutsen, D. Vandezande, P. Heremans, *Appl. Phys. Lett.* **2006**, *89*, 223 504.
[30] J. Zaumseil, R. H. Friend, H. Sirringhaus, *Nat. Mater.* **2006**, *5*, 69.
[31] J. Zaumseil, C. L. Donley, J. Kim, H. Friend, H. Sirringhaus, *Adv. Mater.* **2006**, *18*, 2708.
[32] M. Muccini, *Nat. Mater.* **2006**, *5*, 605.
[33] T. Oyamada, H. Uchiuzou, S. Akiyama, Y. Oku, N. Shimoji, K. Matsushige, H. Sasabe, C. Adachi, *J. Appl. Phys.* **2005**, *98*, 074 506.
[34] Y. Y. Lin, D. J. Gundlach, S. F. Nelson, T. N. Jackson, *IEEE Electron Device Lett.* **1997**, *18*, 606.
[35] H. Sirringhaus, P. J. Brown, R. H. Friend, M. M. Nielsen, K. Bechgaard, B. M. W. Langeveld-Voss, A. J. H. Spiering, R. A. J. Janssen, E. W. Meijer, P. Herwig, D. M. de Leeuw, *Nature* **1999**, *401*, 685.
[36] I. D. W. Samuel, G. Rumbles, C. J. Collison, R. H. Friend, S. C. Moratti, A. B. Holmes, *Synth. Met.* **1997**, *84*, 497.
[37] M. Muratsubaki, Y. Furukawa, T. Noguchi, T. Ohnishi, E. Fujiwara, H. Tada, *Chem. Lett.* **2004**, *33*, 1480.
[38] J. Kido, Y. Lizumi, *Appl. Phys. Lett.* **1998**, *73*, 2721.
[39] C. Adachi, M. A. Baldo, M. E. Thompson, S. R. Forrest, *J. Appl. Phys.* **2001**, *90*, 5048.
[40] S. De Vusser, S. Steudel, K. Mymy, D. Janssen, S. De Jonge, J. Genoe, P. Heremans, *Appl. Phys. Lett.* **2006**, *88*, 103 501.
[41] J. Veres, S. Ogier, S. Leeming, B. Brown, D. Cupertino, *Mater. Res. Soc. Symp. Proc.* **2002**, *708*, BB8.7.1.
[42] V. Bulovic, A. Shoustikov, M. A. Baldo, E. Bose, V. G. Kozlov, M. E. Thompson, S. R. Forrest, *Chem. Phys. Lett.* **1998**, *287*, 455.
[43] C. W. Tang, S. A. VanSlyke, C. H. Chen, *J. Appl. Phys.* **1989**, *65*, 3610.
[44] D. J. Gundlach, K. P. Pernstich, G. Wilckens, M. Grüter, S. Haas, B. Batlogg, *J. Appl. Phys.* **2005**, *98*, 064 502.
[45] S. Tatemichi, M. Ichikawa, T. Koyama, Y. Taniguchi, *Appl. Phys. Lett.* **2006**, *89*, 112 108.
[46] M. A. Baldo, M. E. Thompson, S. R. Forrest, *Pure Appl. Chem.* **1999**, *71*, 2095.
[47] Y. Hamada, H. Kanno, T. Tsujioka, H. Takahashi, T. Usuki, *Appl. Phys. Lett.* **1999**, *75*, 1682.
[48] C. Rost, D. J. Gundlach, S. Karg, W. Rieß, *J. Appl. Phys.* **2004**, *95*, 5782.
[49] T. van Woudenbergh, P. W. M. Blom, J. N. Huiberts, *Appl. Phys. Lett.* **2003**, *82*, 985.
[50] T. W. Kelley, D. V. Muyres, P. F. Baude, T. P. Smith, T. D. Jones, *Mater. Res. Soc. Symp. Proc.* **2003**, *771*, L6.5.1.
[51] L. Chua, J. Zaumseil, J. Chang, E. C. Ou, P. K. Ho, H. Sirringhaus, R. H. Friend, *Nature* **2005**, *434*, 194.
[52] S. Lamansky, P. Djurovich, D. Murphy, F. Abdel-Razzaq, H. Lee, C. Adachi, P. E. Burrows, S. R. Forrest, M. E. Thompson, *J. Am. Chem. Soc.* **2001**, *123*, 4304.
[53] I. Sokolik, R. Priestley, A. D. Walser, R. Dorsinville, C. W. Tang, *Appl. Phys. Lett.* **1996**, *69*, 4168.